Journal of Materials Chemistry C

ROYAL SOCIETY OF CHEMISTRY

PAPER

View Article Online
View Journal | View Issue

Cite this: J. Mater. Chem. C, 2024, 12, 7588

Thermally enhanced NIR up-conversion fluorescence multimode thermometry based on $Y_2Mo_3O_{12}:Nd^{3+},Yb^{3+}$†

Yexuan Zhang,[a] Minkun Jin,[a] Wang Chen,[a] Ziyang Wu,[a] Zexun Li[a] and Chongfeng Guo *[ab]

Received 3rd April 2024,
Accepted 29th April 2024

DOI: 10.1039/d4tc01352b

rsc.li/materials-c

Severe thermal quenching of fluorescence is the main obstacle to the application of fluorescence thermometers in higher temperature regions. In order to broaden the temperature detection range of fluorescence thermometers, the $Y_2Mo_3O_{12}:Nd^{3+},Yb^{3+}$ phosphor with negative thermal expansion (NTE) characteristics was successfully synthesized. The up-conversion (UC) fluorescence thermal enhancement ($^4F_{3/2} \rightarrow {}^4I_{9/2}$) increased 109 times at 480 K and the UC fluorescence lifetime (FL) of the transition $^4F_{5/2} \rightarrow {}^4I_{9/2}$ increased from 77 to 144.5 μs in the range of 280 to 380 K under the excitation of a 980 nm laser. Herein, a multimode temperature probe was constructed through fluorescence intensity ratio (FIR) technology ($^4F_{7/2}/{}^4F_{5/2}$, $^4F_{7/2}/{}^4F_{3/2}$ and $^4F_{5/2}/{}^4F_{3/2}$) and FL technology based on the ladder-like thermally coupled energy levels (TCLs) of Nd^{3+}. The feasibility of the probe was verified and $Y_2Mo_3O_{12}:Nd^{3+},Yb^{3+}$ has high stability and accuracy (δT = 0.61 K at 480 K), indicating that it is an ideal candidate in higher temperature monitoring. This work not only proposes an ideal scheme for designing high sensitivity fluorescence thermometers, but also provides a certain reference value for solving the problem of fluorescence thermal quenching.

1. Introduction

The accurate measurement of temperature has always been a constant pursuit because temperature is one of the vital parameters in human life, modern industry and scientific research. Traditional thermal expansion, thermocouples and thermal resistance thermometers have been unable to meet the requirements of some special conditions such as biological tissues and corrosive environments.[1–4] Non-contact optical fluorescence thermometers based on lanthanide (Ln) or transition metal ion doped luminescent materials were paid more attention in recent years due to their fast response, controllable size and high thermal resolution.[5–8] Among them, thermometers based on the fluorescence intensity ratio (FIR) technology of thermally coupled energy levels (TCLs) have gained more attention due to their stability and repeatability.[9–11] However, severe thermal quenching of fluorescence has restricted their applications in higher temperature ranges. Due to the gradually intensified thermal vibration inside crystals when the temperature rises, more energy of electrons on excited state energy levels is consumed in the way of non-radiative relaxation (NR), which weakens the fluorescence intensity and undoubtedly causes the increase of difficulty and error during the course of temperature detection.[12,13]

Although a lot of works have been done for combating the thermal quenching, including surface engineering (passivation or ligand coordination), high-power excitation, phonon-assisted energy transfer (PAET), *etc.*, only limited success has been achieved due to different difficulties faced by each method and non-universality.[14–16] In recent years, negative thermal expansion (NTE) based luminescent materials showed good prospects in anti-thermal quenching due to their fascinating luminescence promoting capability from structures. Specifically, the microscopic volume of NTE materials will decrease with the increase of temperature and the gradually compact lattice reduces the phonon energy corresponding to the various vibration modes, which can reduce the energy loss caused by NR.[17–19] Among the reported NTE materials, the $A_2M_3O_{12}$ (A = Y, Lu, Yb, Sc; M = W, Mo) family has attracted attention due to their high tolerance to Ln^{3+}, which promote the development and utilization of rare earth doped NTE-based thermometers through the FIR technology.[20–24] However, the temperature probe based on FIR technology has a large error

[a] State Key Laboratory of Photon-Technology in Western China Energy, Institute of Photonics & Photon-Technology, Northwest University, Xi'an 710127, China. E-mail: guocf@nwu.edu.cn; Fax: ±86-29-88302661; Tel: +86-29-88302661
[b] College of Chemistry and Chemical Engineering, Jiangxi Normal University, Nanchang, 330022, China

† Electronic supplementary information (ESI) available. See DOI: https://doi.org/10.1039/d4tc01352b

because different media absorb light with different wavelengths, which promotes the development of thermometers based on different mechanisms.[25–28] Fascinatingly, fluorescence lifetime (FL) technology depends on a great variety of temperature-related factors (such as PAET and the multi-phonon decay process), which makes it possible to obtain temperature information from FL.[29] Specifically, FL originates from the electronic de-excitation kinetics and exhibits a better anti-disturbance ability, not subject to excitation intensity, phosphor concentration and emission loss, which enables it to avoid errors in different measurement situations and carry out calibrations to temperature readouts of FIR technology.[30]

The luminescence of Nd^{3+} has been significantly improved through a PAET process in Yb^{3+} and Nd^{3+} co-doped phosphors under the excitation of a 980 nm laser, which is attributed to the appropriate energy gap ($\sim$1000 cm^{-1}) between the excited state energy levels $^2F_{5/2}$ of Yb^{3+} and $^4F_{3/2}$ of Nd^{3+}.[31] In addition, the near infrared (NIR) fluorescence of ladder-like TCLs ($^4F_{7/2}$, $^4F_{5/2}$ and $^4F_{3/2}$) in Nd^{3+} has a tendency of thermal enhancement with appropriate PAET as the temperature rises,[32] which enabled a high possibility of FL extension of $^4F_{7/2}$, $^4F_{5/2}$ and $^4F_{3/2}$ energy levels with the increase of temperature. Accordingly, NIR fluorescence Nd^{3+}-based thermometers with greater penetrability are ideal candidates for temperature measurements in higher temperature ranges. Fortunately, the phonon energy of $Y_2M_3O_{12}$ is close to the energy mismatch between Yb^{3+} and Nd^{3+}. By selecting appropriate TCLs, the suitable phonon energy and the excellent NTE properties of $Y_2M_3O_{12}$ ($\alpha_V \sim -3.78 \times 10^{-5}$ K^{-1}) make the outstanding FIR and FL temperature sensing performance of Nd^{3+} possible.

Inspired by the above findings, a thermally enhanced multi-mode fluorescence thermometer based on the NTE material $Y_2Mo_3O_{12}$:Nd^{3+},Yb^{3+} was designed in this work. The up-conversion (UC) fluorescence intensity of ladder-like TCLs ($^4F_{7/2} \rightarrow {}^4I_{9/2}$, $^4F_{5/2} \rightarrow {}^4I_{9/2}$ and $^4F_{3/2} \rightarrow {}^4I_{9/2}$) is enhanced 109, 26 and 7 times, and their relevant UC FL ($^4F_{5/2} \rightarrow {}^4I_{9/2}$) is increased from 77 to 144.5 μs, which enable us to construct thermally enhanced fluorescence thermometers based on FIR and FL technologies. By combining the NTE properties of $Y_2Mo_3O_{12}$ with the PAET mechanism between Yb^{3+} and Nd^{3+}, the corresponding optical thin film is proved to have qualified temperature sensing capability and its application range extends to higher temperatures while maintaining excellent performance, which makes it an ideal candidate in higher temperature monitoring.

2. Experimental details

2.1. Synthesis of samples

The $Y_2Mo_3O_{12}$:Nd^{3+},Yb^{3+} powder samples were synthesized using a high-temperature solid-state reaction method. The starting materials, including Y_2O_3 (99.99%), Nd_2O_3 (99.99%), Yb_2O_3 (99.99%) and MoO_3 (99.9%), were first weighed according to a certain stoichiometric ratio and mixed completely. Then, the mixture was calcined in a muffle furnace at 850 °C for 6 h and the final samples were successfully obtained after naturally cooling down to room temperature.

2.2. Characterization

The phase purity and crystal structures of all the prepared samples were determined using a powder X-ray diffractometer (XRD) with Cu Kα radiation (Rigaku Corporation, Tokyo, Japan; λ = 1.54056 Å) in the range of $10^\circ \leq 2\theta \leq 80^\circ$. The Fourier transform infrared (FT-IR) spectra and Raman spectra were collected on a Bruker INVENIO-R spectrometer and a Thermo Fisher DXR2 laser confocal microscopy Raman spectrometer, respectively. The temperature-dependent UC emission spectra and FL spectra were recorded on a fluorescence spectrometer (Edinburgh FLS920) with a liquid nitrogen cryogenic temperature-control system (Oxford OptistatDN2) combined with an external power-adjustable 980 nm semiconductor laser.

3. Results and discussion

3.1. Crystal structure analysis

In order to prove the phase purity of the samples, XRD patterns of $Y_2Mo_3O_{12}$:1% Nd^{3+},y% Yb^{3+} were measured and are displayed in Fig. 1a and Fig. S1 (ESI†). All diffraction peaks of doped and undoped (blank) samples were consistent with those of the standard profiles of orthorhombic $Y_2Mo_3O_{12}$ (JCPDS#28-1451) with the *Pbcn* (60) space group. The FT-IR and Raman spectra were recorded to obtain the lattice vibration information to determine the phonon energy of the doped and blank samples. As shown in Fig. 1b, FT-IR spectra of both blank and doped samples show the strongest absorption peak at 866 cm^{-1}, which corresponds to the vibration of Mo–O–Mo. The bands centered at 1612 cm^{-1} and 3368 cm^{-1} are attributed to the stretching vibration of O–H. As shown in Fig. 1c, the peak at 340 cm^{-1} in the Raman spectra is attributed to symmetric and asymmetric bending motions in both the YO_6 octahedron and the MoO_4 tetrahedron. The strongest peaks at 815 cm^{-1} and 952 cm^{-1} are attributed to the asymmetric and symmetric stretching vibrations of the MoO_4 tetrahedra.[33–35] From the above analysis, it can be seen that the phonon energy of the samples is 952 cm^{-1}, which is close to the energy mismatch between Nd^{3+} and Yb^{3+}. As shown in Fig. 1d and e, Rietveld XRD refinements were performed to further confirm the phase purity of the doped and blank samples, and the corresponding results are shown in Table S1 (ESI†). In addition, the results show that the lattice volume (V) of the doped sample is smaller than that of the blank sample due to the substitution of Y^{3+} ions with larger ionic radii by smaller Yb^{3+} ions. $Y_2Mo_3O_{12}$ crystallized in an orthorhombic system and its crystal structure diagram is shown in Fig. 1f, in which the YO_6 octahedron and the MoO_4 tetrahedron are connected an oxygen atom.[36] Furthermore, Nd^{3+} (0.983 Å) and Yb^{3+} (0.868 Å) are more inclined to occupy the Y^{3+} (0.900 Å) position due to the close ionic radii and the same valence state.

3.2. Negative thermal expansion analysis

For further determining how the crystal structure of $Y_2Mo_3O_{12}$ changes with temperature, temperature-dependent XRD was

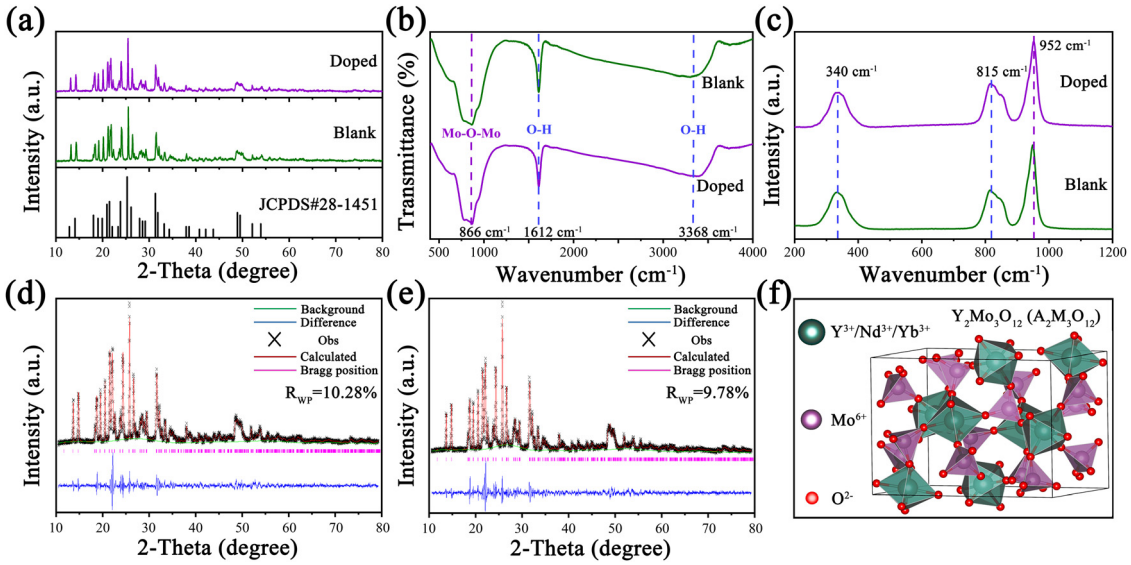

Fig. 1 (a) XRD patterns, (b) FT-IR spectra and (c) Raman spectra of $Y_2Mo_3O_{12}$ and $Y_2Mo_3O_{12}$:1% Nd^{3+},5% Yb^{3+} together with the Rietveld XRD refinements of (d) $Y_2Mo_3O_{12}$ and (e) $Y_2Mo_3O_{12}$:1% Nd^{3+},5% Yb^{3+}. (f) Crystal structure diagram of $Y_2Mo_3O_{12}$.

performed and the results are displayed in Fig. 2a. With the temperature increasing from 80 to 380 °C, no significant variations were observed in the XRD patterns of the sample, indicating that there is no phase change with the increase of temperature. However, obvious peak shifts to larger angles were found when the peaks corresponding to the lattice planes of (220) and (111) were amplified, as shown in Fig. 2b and c, respectively. According to Bragg's law ($2d\sin\theta = n\lambda$), the shifted peaks prove that $Y_2Mo_3O_{12}$ has a lattice shrinkage with the increase of temperature, and the shrinkage diagram is displayed in Fig. 2d. The transverse vibration of the bridging oxygen atom intensifies gradually with the increase of temperature, and then the lattice rotates and shrinks. When the temperature rises, the gradually compact lattice weakens the lattice vibration amplitude and thus weakens the energy loss caused by NR, which may affect the luminescence of Ln^{3+} doped in it.

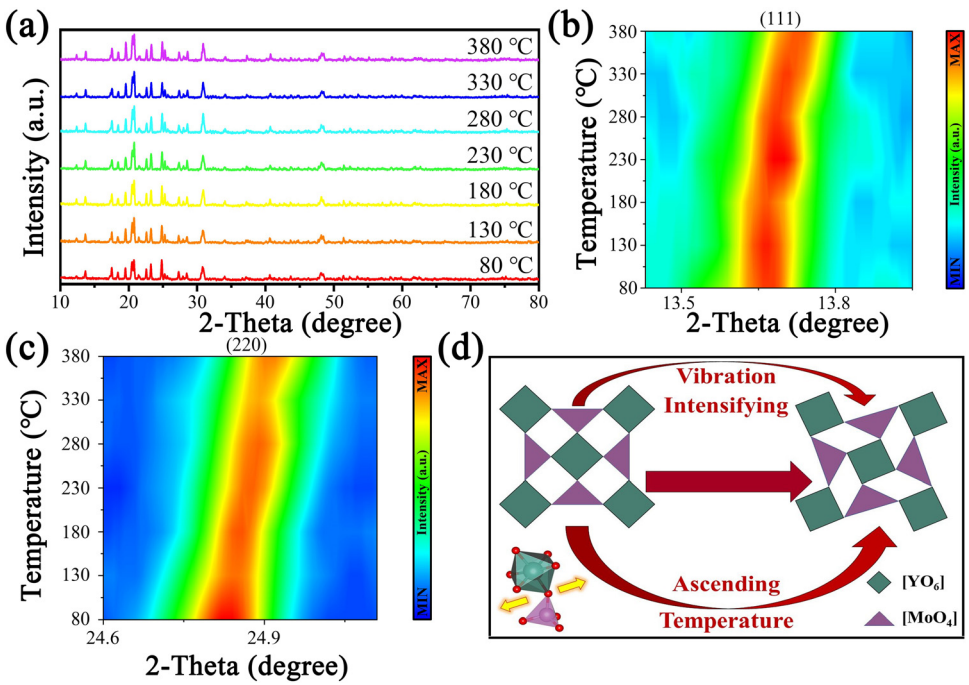

Fig. 2 Temperature-dependent (a) XRD patterns of $Y_2Mo_3O_{12}$ and two-dimensional mapping of diffraction peaks (b) (111) and (c) (220) as well as (d) lattice distortion diagram of $Y_2Mo_3O_{12}$.

3.3. UC luminescence characteristics

The UC spectra of $Y_2Mo_3O_{12}$:1% Nd^{3+},*y*% Yb^{3+} with 980 nm laser excitation are displayed in Fig. 3a, which include the emissions of $^4F_{7/2} \rightarrow {}^4I_{9/2}$ (725–775 nm, I_1), $^4F_{5/2} \rightarrow {}^4I_{9/2}$ (776–840 nm, I_2) and $^4F_{3/2} \rightarrow {}^4I_{9/2}$ (841–885 nm, I_3), and the corresponding fluorescence intensities increase with increasing doping concentration of Yb^{3+} in our experimental range. To determine the UC mechanism, the dual logarithmic fitting curves of UC emission integral intensities (I) of $^4F_{7/2} \rightarrow {}^4I_{9/2}$, $^4F_{5/2} \rightarrow {}^4I_{9/2}$ and $^4F_{3/2} \rightarrow {}^4I_{9/2}$ emission bands related to pumping power (P) were recorded and are displayed in Fig. S2 (ESI†). The slopes (n = 0.68, 0.53 and 0.27) of the fitting curves denote the dominant role of one photon in the UC process according to the relationship: $I \propto P^n$ and the possible UC processes of $Y_2Mo_3O_{12}$:1% Nd^{3+},5% Yb^{3+} under 980 nm laser excitation are displayed in Fig. 3b. Electrons on the ground state energy level $^2F_{7/2}$ (Yb^{3+}) jump to the excited state energy level $^2F_{5/2}$ (Yb^{3+}) by absorbing a 980 nm photon, and then the energy was transferred to Nd^{3+} with the aid of phonon energy. Consequently, electrons on the ground state energy level $^4I_{9/2}$ (Nd^{3+}) jump to the excited state energy level $^4F_{3/2}$ (Nd^{3+}), which is called PAET-1. On the other hand, part of the energy generated by Yb^{3+} is possibly consumed by phonon energy, and the rest of the energy is transferred to Nd^{3+} to promote jumping of electrons on $^4I_{9/2}$ to the excited state energy level $^4I_{15/2}$ (Nd^{3+}), which is called PAET-2. Meanwhile, the electrons populated on $^4I_{15/2}$ jump to $^2H_{11/2}$ (Nd^{3+}) through absorption of a 980 nm photon or ET from Yb^{3+}, which is called ET-3. Then the electrons on $^2H_{11/2}$ relax downward to $^4F_{3/2}$ by successive NR ($^2H_{11/2} \rightarrow {}^4F_{7/2} \rightarrow {}^4F_{5/2} \rightarrow {}^4F_{3/2}$), generating emissions around 747, 808 and 848 nm from transitions $^4F_{7/2} \rightarrow {}^4I_{9/2}$, $^4F_{5/2} \rightarrow {}^4I_{9/2}$ and $^4F_{3/2} \rightarrow {}^4I_{9/2}$, respectively. Because the energy level gaps between $^4F_{7/2}$ and $^4F_{5/2}$ ($\sim$887 cm^{-1}) and $^4F_{5/2}$ and $^4F_{3/2}$ ($\sim$1316 cm^{-1}) fall in the range of 200–2000 cm^{-1} and belong to TCLs, the number of electrons on the upper energy level will increase, while the number of electrons on the lower energy level will decrease with the increase of temperature by following the Boltzmann distribution. The population of the energy level $^4F_{3/2}$ will increase with the increase of temperature because the energy mismatch between Yb^{3+} and Nd^{3+} is supplemented by the more and more popular occurrence of PAET, resulting in an enhancement of 848 nm emission from transition $^4F_{3/2} \rightarrow {}^4I_{9/2}$ in the phosphor $Y_2Mo_3O_{12}$:1% Nd^{3+},5% Yb^{3+}.

In order to explore the temperature sensing performance of the present sample $Y_2Mo_3O_{12}$:1% Nd^{3+},5% Yb^{3+}, its temperature-dependent UC spectra were recorded and are displayed in Fig. 3c. With the temperature increasing from 280 to 480 K, the overall fluorescence intensity of $Y_2Mo_3O_{12}$:1% Nd^{3+},5% Yb^{3+} continues to increase and the integral fluorescence intensities of I_1, I_2 and I_3 were enhanced 109, 26 and 7 times at 480 K in comparison with those at 280 K, respectively, as shown in Fig. 3d and Fig. S3 (ESI†). In addition, the temperature-dependent down-conversion (DC) spectra of $Y_2Mo_3O_{12}$:1% Nd^{3+},5% Yb^{3+} were also compared with those of other Nd^{3+} and Yb^{3+} doped materials under 808 nm laser excitation, and the DC spectra of the present sample showed a significant

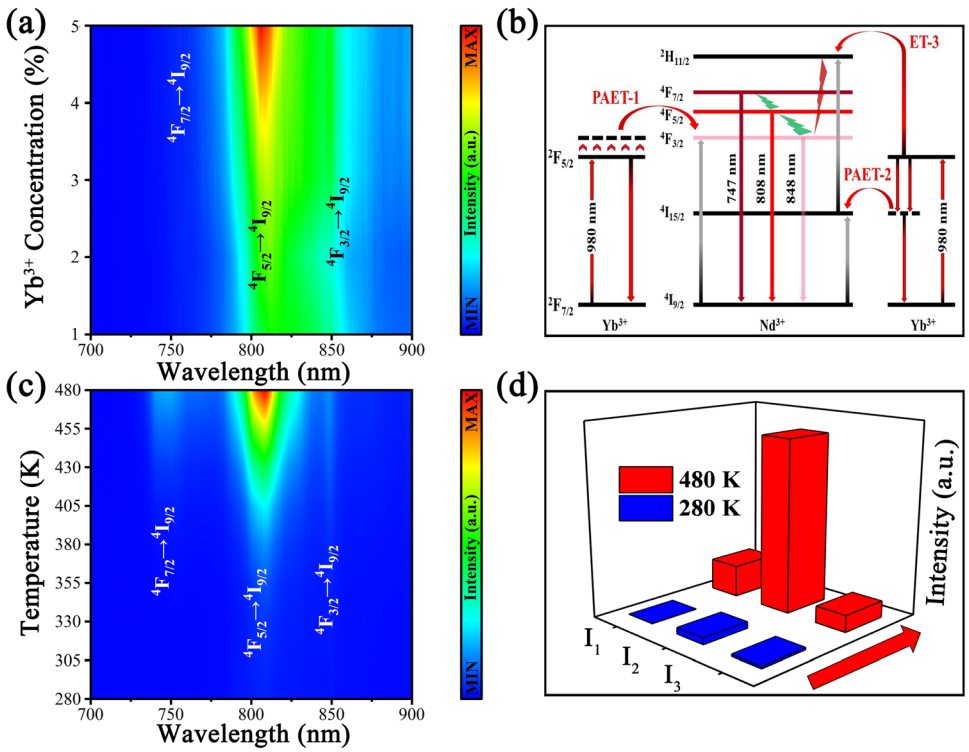

Fig. 3 (a) UC spectra of $Y_2Mo_3O_{12}$:1% Nd^{3+},*y*% Yb^{3+}. (b) Possible UC processes of $Y_2Mo_3O_{12}$:1% Nd^{3+},5% Yb^{3+} under 980 nm laser excitation. (c) Temperature-dependent UC spectra and (d) thermal enhancement comparison of ladder-like TCLs of Nd^{3+} at 280 and 480 K.

fluorescence thermal enhancement with the temperature rising from 330 to 480 K (in Fig. S4a, ESI†), but other materials generally showed a trend of thermal quenching.[37–39] The possible DC processes of $Y_2Mo_3O_{12}$:1% Nd^{3+},5% Yb^{3+} under 808 nm laser excitation are displayed in Fig. S4b (ESI†). It is reasonable to believe that the special NTE properties of the $Y_2Mo_3O_{12}$ matrix indeed make the UC or DC fluorescence of $Y_2Mo_3O_{12}$:1% Nd^{3+},5% Yb^{3+} show a special thermal enhancement trend.

3.4. Optical thermometric performance

Due to the excellent temperature-dependent properties of $Y_2Mo_3O_{12}$:1% Nd^{3+},5% Yb^{3+} and the different increasing rates of different emissions, its temperature sensing capability was continuously evaluated. The FIR temperature sensing property of $Y_2Mo_3O_{12}$:1% Nd^{3+},5% Yb^{3+} could be defined according to formula (1):[40–43]

$$\mathrm{FIR} = \frac{I_x}{I_y} = \frac{N_1\hbar\omega_1 A_1}{N_2\hbar\omega_2 A_2} = \frac{\omega_1 A_1 g_1}{\omega_2 A_2 g_2} \cdot \exp\left(-\frac{\Delta E}{k_B T}\right) \quad (1)$$

where I_x and I_y are the different fluorescence integral intensities emitted by TCLs, respectively; N, ω, A and g are the number of electrons corresponding to TCLs, frequency, spontaneous emission probability and energy level degeneracy, respectively; ΔE, $\hbar$, k_B and T are the energy gap between TCLs, the reduced Planck constant, the Boltzmann constant and absolute temperature, respectively. Sensitivity including relative (S_R) and absolute (S_A) is an important parameter to evaluate the performance of FIR thermometers, which were defined using formulas (2) and (3):[44–46]

$$S_R = \left|\frac{1}{\mathrm{FIR}} \times \frac{\mathrm{d(FIR)}}{\mathrm{d}T}\right| = \frac{\Delta E}{k_B T^2} \quad (2)$$

$$S_A = \left|\frac{\mathrm{d(FIR)}}{\mathrm{d}T}\right| = \mathrm{FIR} \times \frac{\Delta E}{k_B T^2} \quad (3)$$

Accordingly, I_1/I_2, I_1/I_3 and I_2/I_3 are set as FIR_1, FIR_2 and FIR_3, respectively. Because the number of electrons on TCLs follows the Boltzmann distribution, the three FIRs of the temperature-dependent UC spectra all increased with the temperature rising from 280 to 480 K, as shown in Fig. 4a–c. Accordingly, the S_R and S_A values of the three thermometers were calculated using formulas (2) and (3), as shown in Fig. 4d–f and Fig. S5a–c (ESI†), reaching a maximum of 3.49% K^{-1} and 0.0518 K^{-1}, which are excellent in the most reported fluorescence thermometers based on FIR technology (Table S2, ESI†). Meanwhile, seven heating and cooling cycles were executed to test the reversibility of the three FIRs, which are displayed in Fig. 4g–i.

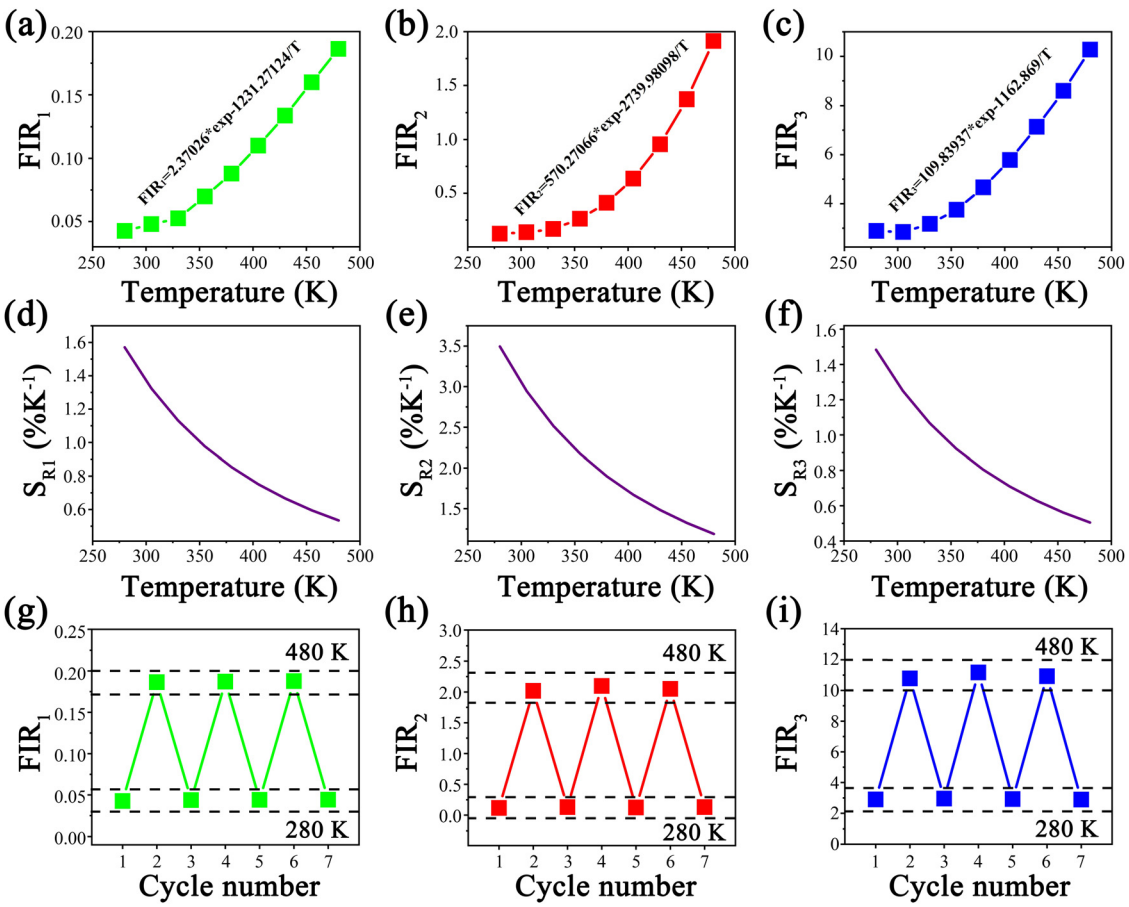

Fig. 4 (a)–(c) Temperature-dependent FIR and fitting curves of FIR_1, FIR_2 and FIR_3. (d)–(f) S_R of the three kinds of FIR. (g)–(i) Heating and cooling cycles of the three kinds of FIR.

The above results proved that the three FIRs based on the temperature-dependent UC spectra of $Y_2Mo_3O_{12}$:1% Nd^{3+},5% Yb^{3+} have excellent repeatability and stability.

In comparison with the fluorescence intensity, FL is not sensitive to the change of excitation source intensity and emission loss, which enables it to avoid errors from the fluorescence inherent in different measurement situations. Considering the high fluorescence intensity and relatively high fluorescence thermal enhancement of the transition $^4F_{5/2} \rightarrow {}^4I_{9/2}$ in the temperature-dependent UC spectra of $Y_2Mo_3O_{12}$:1% Nd^{3+},5% Yb^{3+}, the temperature sensing capability of its UC FL (808 nm) was further explored. The FL decay curve could be well fitted using formula (4):

$$I = A_1 \exp\left(\frac{-t}{\tau_1}\right) + A_2\left(\frac{-t}{\tau_2}\right) + I_0 \quad (4)$$

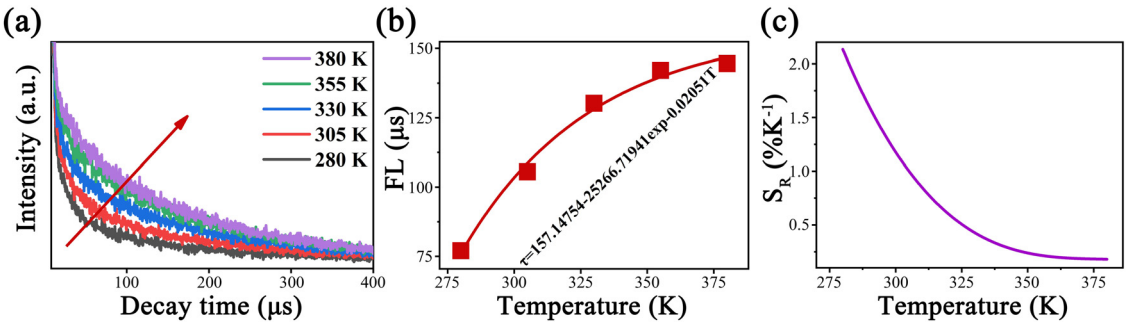

Fig. 5 Temperature-dependent (a) decay curves of the excited state energy level $^4F_{5/2}$, (b) FL and fitting curve, and (c) S_R of the FL of $Y_2Mo_3O_{12}$:1% Nd^{3+},5% Yb^{3+} under 980 nm laser excitation.

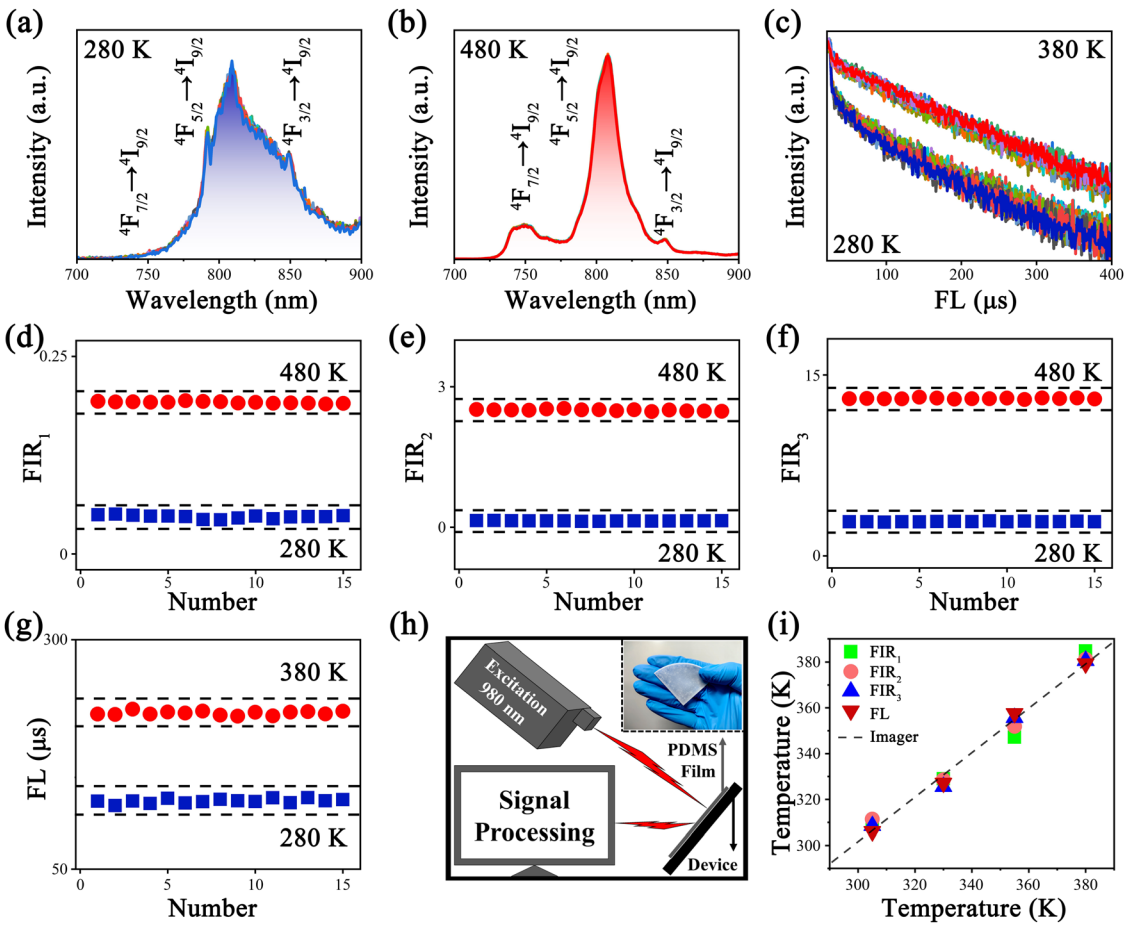

Fig. 6 (a) and (b) 15 records of UC spectra of $Y_2Mo_3O_{12}$:1% Nd^{3+},5% Yb^{3+} at 280 and 480 K. (c) 15 records of decay curves of the excited state energy level $^4F_{5/2}$ at 280 and 380 K. (d)–(g) Calculation results of the three kinds of FIR and FL at different temperatures. (h) Schematic diagram of film non-contact temperature sensing. (i) Temperature readout comparison of the four kinds of thermometers with a thermal imager.

where I and I_0 are the fluorescence intensities when the time is t and 0, respectively. A_1, A_2, τ_1 and τ_2 are the fitting constants to be determined.[47,48] Meanwhile, the average FL and its functional relationship with temperature could be well fitted using formulas (5) and (6):[49,50]

$$\tau = \frac{A_1\tau_1^2 + A_2\tau_2^2}{A_1\tau_1 + A_2\tau_2} \quad (5)$$

$$\tau = y_0 + A\cdot\exp(R_0\cdot T) \quad (6)$$

where y_0, A and R_0 are the fitting constants to be determined. τ and T are the average FL and absolute temperature, respectively. Similarly, the performance of the FL thermometer is evaluated by S_R which was defined using formula (7):

$$S_R = 100\% \times \left|\frac{1}{\tau}\times\frac{\partial\tau}{\partial T}\right| \quad (7)$$

As shown in Fig. 5a and b, the FL (808 nm) of $Y_2Mo_3O_{12}$:1% Nd^{3+},5% Yb^{3+} extended continually with the temperature rising from 280 to 380 K, and the fitting average FL is prolonged from 77 to 144.5 μs. As the temperature increased, the number of electrons on $^4F_{5/2}$ continued to increase, and the average FL of the transition $^4F_{5/2} \rightarrow {}^4I_{9/2}$ was prolonged. Accordingly, the S_R value of the FL thermometer was calculated using formula (7), as shown in Fig. 5c, reaching a maximum of 2.13% K^{-1}, which is comparable to those of most reported fluorescence thermometers based on FIR technology (Table S2, ESI†). The above results proved that the temperature-dependent UC FL based on the transition $^4F_{5/2} \rightarrow {}^4I_{9/2}$ of $Y_2Mo_3O_{12}$:1% Nd^{3+},5% Yb^{3+} has a competent temperature sensing capability.

In practical temperature measurements, qualified temperature resolution (δT) is more important in addition to excellent sensitivity. In order to determine the minimum temperature change that can be detected by FIR and FL thermometers, the δT was evaluated according to the formula $\delta T = \delta\mathrm{FIR}/(\mathrm{FIR}^{*}S_R)$.[51] As shown in Fig. 6a–c, the UC spectra and FL decay curves of $Y_2Mo_3O_{12}$:1% Nd^{3+},5% Yb^{3+} were recorded 15 times under the same measurement settings, and the corresponding calculation results are shown in Fig. 6d–g, respectively. The best δT values reached 0.57 K at 280 K and 0.61 K at 480 K, and the results showed that the δT of thermometers did not deteriorate severely after fluorescence thermal enhancement (Table S3, ESI†).

Based on the corresponding high sensitivity FIR and FL of $Y_2Mo_3O_{12}$:1% Nd^{3+},5% Yb^{3+}, its practical application was also evaluated by building an ultra-sensitive flexible thin film temperature sensor through mixing the $Y_2Mo_3O_{12}$:1% Nd^{3+},5% Yb^{3+} phosphor with polydimethylsiloxane (PDMS).[52–55] As a demonstration of the working process, its working diagram for real-time temperature sensing of precision devices is displayed in Fig. 6h. The FIR and FL of the phosphor were monitored, and the corresponding environmental temperature could be obtained according to the fitting curves, which is displayed in Fig. S6a–d (ESI†). As shown in Fig. 6i, the temperature measurement results of four kinds of thermometers were basically consistent with a thermal imager, which proved that the multimode thermometer has an accurate temperature sensing capability and self-calibration function. Meanwhile, $Y_2Mo_3O_{12}$:1% Nd^{3+},5% Yb^{3+} has better temperature sensing performance compared with most existing thermometers based on Nd^{3+} and the non-NTE matrix (Table S2, ESI†).

4. Conclusions

The NTE material $Y_2Mo_3O_{12}$:1% Nd^{3+},5% Yb^{3+} was successfully synthesized using a high-temperature solid-state reaction method and the possible UC processes under the excitation of a 980 nm laser were analyzed in detail. By combining the NTE properties of $Y_2Mo_3O_{12}$ with the PAET mechanism between Yb^{3+} and Nd^{3+}, the UC fluorescence thermal enhancement ($^4F_{3/2} \rightarrow {}^4I_{9/2}$) by 109 times at 480 K and UC FL thermal extension ($^4F_{5/2} \rightarrow {}^4I_{9/2}$) from 77 to 144.5 μs in the NIR region were achieved. According to the temperature-dependent UC spectra and FL decay curves of $Y_2Mo_3O_{12}$:1% Nd^{3+},5% Yb^{3+}, a multimode high sensitivity fluorescence thermometer was designed by combining three kinds of FIRs ($^4F_{7/2}/^4F_{5/2}$, $^4F_{7/2}/^4F_{3/2}$ and $^4F_{5/2}/^4F_{3/2}$) with the FL ($^4F_{5/2} \rightarrow {}^4I_{9/2}$) of Nd^{3+}. The optimal S_R and δT values of $Y_2Mo_3O_{12}$:1% Nd^{3+},5% Yb^{3+} reached 3.49% K^{-1} and 0.57 K at 280 K, respectively. Meanwhile, the corresponding optical thin film is proved to have an accurate temperature sensing capability and self-calibration function. It is expected to have ideal application prospects as a NIR fluorescence thermally enhanced multimode thermometer in higher temperature environments.

Author contributions

Y. Zhang conducted most of the experiments and their analyses with the assistance of M. Jin and W. Chen, and wrote the manuscript under the supervision of C. Guo. Z. Wu assisted in Rietveld XRD refinements and calculations of the lattice parameters. Z. Li assisted in optical thin film preparation.

Conflicts of interest

The authors declare no competing financial interests.

Acknowledgements

This work was supported by the National Natural Science Foundation of China (No. 11974278, 51672215, and 12104367) and the Youth Innovation Team of Shaanxi Universities and Thousand Talents Plan of Jiangxi Province (jxsq2020102064).

References

1 X. Wang, O. S. Wolfbeisa and R. J. Meier, *Chem. Soc. Rev.*, 2013, **42**, 7834–7869.
2 C. Mi, J. Zhou, F. Wang, G. Lin and D. Jin, *Chem. Mater.*, 2019, **31**, 9480–9487.

3 M. Runowski, N. Stopikowska, D. Szeremeta, S. Goderski, M. Skwierczyńska and S. Lis, *ACS Appl. Mater. Interfaces*, 2019, **11**, 13389–13396.
4 E. Pavitra, H. Lee, S. K. Hwang, J. Y. Park, G. L. Varaprasad, M. V. B. Rao, Y. K. Han, G. S. R. Raju and Y. S. Huh, *Appl. Surf. Sci.*, 2022, **579**, 152166.
5 C. D. S. Brites, P. P. Lima, N. J. O. Silva, A. Millán, V. S. Amaral, F. Palacio and L. D. Carlos, *Nanoscale*, 2012, **4**, 4799–4829.
6 H. Suo, X. Zhao, Z. Zhang, Y. Wang, J. Sun, M. Jin and C. Guo, *Laser Photonics Rev.*, 2020, **15**, 2000319.
7 X. Qiu, Q. Zhou, X. Zhu, Z. Wu, W. Feng and F. Li, *Nat. Commun.*, 2020, **11**, 4.
8 M. Sojka, W. Piotrowski, L. Marciniak and E. Zych, *J. Alloys Compd.*, 2024, **970**, 172662.
9 C. D. S. Brites, S. Balabhadra and L. D. Carlos, *Adv. Opt. Mater.*, 2019, **7**, 1801239.
10 A. A. Ansari, A. K. Parchur, M. K. Nazeeruddin and M. M. Tavakoli, *Coord. Chem. Rev.*, 2021, **444**, 214040.
11 M. Jia, X. Chen, R. Sun, D. Wu, X. Li, Z. Shi, G. Chen and C. Shan, *Nano Res.*, 2023, **16**, 2949–2967.
12 A. M. Kaczmarek, M. Suta, H. Rijckaert, A. Abalymov, I. V. Driessche, A. G. Skirtach, A. Meijerink and P. V. D. Voort, *Adv. Funct. Mater.*, 2020, **30**, 2003101.
13 Q. Li, X. Xie, H. Wu, H. Chen, W. Wang, X. Kong and Y. Chang, *Nano Lett.*, 2023, **23**, 3444–3450.
14 J. Zhou, S. Wen, J. Liao, C. Clarke, S. A. Tawfik, W. Ren, C. Mi, F. Wang and D. Jin, *Nat. Photonics*, 2018, **12**, 154–158.
15 H. Xu, S. Han, R. Deng, Q. Su, Y. Wei, Y. Tang, X. Qin and X. Liu, *Nat. Photonics*, 2021, **15**, 732–737.
16 D. Zhang, J. Zhou, X. Cao, X. Ge, F. Tang, C. Zheng, J. Ning and S. Xu, *J. Phys. Chem. Lett.*, 2023, **14**, 6464–6469.
17 H. Zou, X. Yang, B. Chen, Y. Du, B. Ren, X. Sun, X. Qiao, Q. Zhang and F. Wang, *Angew. Chem., Int. Ed.*, 2019, **58**, 17255–17259.
18 L. Chen, X. Chen, R. Ma, K. Lin, Q. Li, J. Lang, C. Liu, K. Kato, L. Huang and X. Xing, *J. Am. Chem. Soc.*, 2022, **144**, 13688–13695.
19 J. Liao, M. Wang, F. Lin, Z. Han, B. Fu, D. Tu, X. Chen, B. Qiu and H. Wen, *Nat. Commun.*, 2022, **13**, 2090.
20 M. T. Dove and H. Fang, *Rep. Prog. Phys.*, 2016, **79**, 066503.
21 H. Zou, B. Chen, Y. Hu, Q. Zhang, X. Wang and F. Wang, *J. Phys. Chem. Lett.*, 2020, **11**, 3020–3024.
22 Y. Wei, Y. Pan, E. Zhou, Z. Yuan, H. Song, Y. Wang, J. Zhou, J. Rui, M. Xu, L. Ning, Z. Liu, H. Wang, X. Xie, X. Tang, H. Su, X. Xing and L. Huang, *Angew. Chem., Int. Ed.*, 2023, **135**, e202303482.
23 Q. Wang, J. Wen, J. Zheng, Q. Xia, C. Wei, X. Huang, Z. Mu and F. Wu, *J. Lumin.*, 2022, **252**, 119306.
24 L. Pu, P. Li, J. Zhao, Y. Wang, D. Guo, L. Li, Z. Wang and H. Suo, *Laser Photonics Rev.*, 2023, **17**, 2200884.
25 Z. Ji, Y. Cheng, X. Cui, H. Lin, J. Xu and Y. Wang, *Inorg. Chem. Front.*, 2019, **6**, 110–116.
26 K. He, L. Zhang, Y. Liu, B. Xu, L. Chen and G. Bai, *J. Alloys Compd.*, 2022, **890**, 161918.
27 M. S. Pudovkin, A. K. Ginkel, O. A. Morozov, A. G. Kiiamov and M. D. Kuznetsov, *J. Lumin.*, 2022, **249**, 119037.
28 K. Chen, Z. Shao, C. Zhang, S. Jia, T. Deng, R. Zhou, Y. Zhou and E. Song, *Chem. Eng. J.*, 2023, **477**, 147165.
29 D. Jaque and F. Vetrone, *Nanoscale*, 2012, **4**, 4301–4326.
30 A. Bednarkiewicz, L. Marciniak, L. D. Carlos and D. Jaque, *Nanoscale*, 2020, **12**, 14405–14421.
31 H. Suo, X. Zhao, Z. Zhang and C. Guo, *Chem. Eng. J.*, 2020, **389**, 124506.
32 L. Pu, Y. Wang, J. Zhao, M. Jin, L. Li, P. Li, Z. Wang, C. Guo and H. Suo, *Chem. Eng. J.*, 2022, **449**, 137890.
33 H. Lv, P. Du, L. Luo and W. Li, *Mater. Adv.*, 2021, **2**, 2642–2648.
34 L. Wang, F. Wang, P. Yuan, Q. Sun, E. Liang, Y. Jia and Z. Guo, *Mater. Res. Bull.*, 2013, **48**, 2724–2729.
35 X. Liu, Y. Cheng, E. Liang and M. Chao, *Phys. Chem. Chem. Phys.*, 2014, **16**, 12848–12857.
36 Y. Yang, L. Lin, P. Lu, Z. Feng, Z. Li, J. Cai, Z. Mei, Y. Huang, W. Guo, Z. Wang and Z. Zheng, *J. Lumin.*, 2021, **240**, 118410.
37 Z. Zhang, M. Jin, L. Yao and C. Guo, *Opt. Mater.*, 2021, **121**, 111607.
38 X. Jiang, Y. Sun, X. Wang, L. Hu, S. Chen and Q. Yang, *J. Lumin.*, 2022, **251**, 119146.
39 C. Gu, Y. Ding, X. Quan, M. Gong, J. Yu, D. Zhao and C. Li, *J. Rare Earth*, 2021, **39**, 1024–1030.
40 S. K. Singh, K. Kumar and S. B. Rai, *Sens. Actuators, A*, 2009, **149**, 16–20.
41 A. Pandey, V. K. Rai, V. Kumar, V. Kumar and H. C. Swart, *Sens. Actuators, B*, 2015, **209**, 352–358.
42 Ž. Antić, M. D. Dramićanin, K. Prashanthi, D. Jovanović, S. Kuzman and T. Thundat, *Adv. Mater.*, 2016, **28**, 7745–7752.
43 Y. Gao, F. Huang, H. Lin, J. Zhou, J. Xu and Y. Wang, *Adv. Funct. Mater.*, 2016, **26**, 3139–3145.
44 H. Suo, F. Hu, X. Zhao, Z. Zhang, T. Li, C. Duan, M. Yin and C. Guo, *J. Mater. Chem. C*, 2017, **5**, 1501–1507.
45 Y. Chen, J. Chen, Y. Tong, W. Zhang, X. Peng, H. Guo and D. Huang, *J. Rare Earths*, 2021, **39**, 1512–1519.
46 Y. Sun, M. Chen, P. Xiong, Y. Wang, S. Tian, Q. Jiang, Y. Xiao, H. Zhou, P. Shao, Q. Zhan, J. Gan, Q. Qian, D. Chen and Z. Yang, *Adv. Powder Mater.*, 2023, **2**, 100132.
47 J. Xiang, J. Zheng, X. Zhao, X. Zhou, C. Chen, M. Jin and C. Guo, *Mater. Chem. Front.*, 2022, **6**, 440–449.
48 M. Jin, Y. Wu, Z. Zhang, J. Xiang and C. Guo, *Opt. Laser Technol.*, 2022, **152**, 108144.
49 H. Suo, C. Guo, Z. Yang, S. Zhou, C. Duan and M. Yin, *J. Mater. Chem. C*, 2015, **3**, 7379–7385.
50 Q. Yang, L. Zhao, Z. Fang, Z. Yang, J. Cao, Y. Cai, D. Zhou, X. Yu, J. Qiu and X. Xu, *J. Rare Earths*, 2021, **39**, 712–717.
51 G. Bao, K. Wong, D. Jin and P. A. Tanner, *Light-Sci. Appl.*, 2018, **7**, 96.
52 J. Tang, Y. Wu, M. Jin, Y. Li, C. Chen, J. Xiang and C. Guo, *Inorg. Chem.*, 2022, **61**, 20035–20042.
53 W. Chen, M. Jin, J. Tang, Y. Li, C. Chen, J. Xiang, Z. Li and C. Guo, *J. Lumin.*, 2023, **263**, 120132.
54 S. Yakunin, B. M. Benin, Y. Shynkarenko, O. Nazarenko, M. I. Bodnarchuk, D. N. Dirin, C. Hofer, S. Cattaneo and M. V. Kovalenko, *Nat. Mater.*, 2019, **18**, 846–852.
55 A. F. Bravo, D. Wang, E. S. Barnard, A. Teitelboim, C. Tajon, J. Guan, G. C. Schatz, B. E. Cohen, E. M. Chan, P. J. Schuck and T. W. Odom, *Nat. Mater.*, 2019, **18**, 1172–1176.